Supplementary Information for

# Metainterface with mechanical, thermal, and active programming based on programmable orientation-distributed biometric architectonics

Zhenyang Gao[1,2], Hongze Wang[1,2,3,4*], Pengyuan Ren[1,2], Gengchen Zheng[1,2], Yang Lu[5], Bokang Peng[1,2], Zijue Tang[1,2], Yi Wu[1,2,3*], Haowei Wang[1,2,3]

[1]State Key Labortory of Metal Matrix Composites, Shanghai Jiao Tong University, Shanghai, 200240, China.
[2]School of Materials Science and Engineering, Shanghai Jiao Tong University, Shanghai, 200240, China.
[3]Institute of Alumics Materials, Shanghai Jiao Tong University (Anhui), Huaibei, 235000, China.
[4]Shanghai Key Laboratory of Material Laser Processing and Modification, Shanghai, 200240, China.
[5]Department of Mechanical Engineering, the University of Hong Kong, Hong Kong, 999077, China.
***Corresponding authors.** E-mail: hz.wang@sjtu.edu.cn, eagle51@sjtu.edu.cn

**This PDF file includes:**

Supplementary Notes 1 to 3
Figures S1 to S30
Tables S1 to S7
Captions for Movies S1 to S7

**Other supporting materials for this manuscript include the following:**

Movies S1 to S7

**Supplementary Note 1.** Design rationales, advantages, and crack extension mechanisms for metainterface.

Programming the interface properties requires highly anisotropic behaviors of the interface design unit. In comparison to various sharp edges found in biological structures [1, 2, 3] (Figure S1), honeybee stinger has evolved with highly anisotropic geometries, characterized by their backward barbs, rendering it an ideal choice for designing interface elements with programmable anisotropic mechanical and dynamical properties [4, 5, 6]. Those stingers have three-dimensional features with limited sizes ranging from micro- to nanoscales [7], making them difficult to observe, reconstruct, and manufacture.

To interpret the underlying mechanisms responsibly for the mechanical advantages of the metainterface featuring XCT-rebuild biostructures in comparison to interfaces with highly simplified biometric geometries, we quantified crack extensions mechanisms (theoretical diagram in Figure S27 (a)) from the substrate to the interface design area using the ZEISS Xradia 520 Versa X-ray microscopic equipment, offering a resolution of 29.203 μm (Figure S27 (b-d) and Supplementary movies Movie S1, also consult Figure S19 and Section 4.5 in Methods for additional details). In contrast to the interfaces with the simplified biometric geometries, it is evident that a greater number of microcracks extend from the substrate to the XCT-rebuild stingers. This mechanism underscores the enhanced effectiveness of XCT-rebuild biostructures in leveraging the rigid interface surface to redistribute mechanical stress and fracture energies during interfacial decoupling, substantiating the mechanical advancements brought about by the XCT-rebuild geometries in this study. The fracture process of the metainterface is simulated using finite element analysis (FEA) as shown in Figure S28. The simulation reveals that the XCT-reconstructed stinger geometry initiates microcracks, which gradually extend to form a major crack leading to complete fracture. This microcracking mechanism allows significant stress distribution to the substrate surrounding the stinger geometry, enhancing the mechanical modulus, strength, and absorbed interfacial energy during the interface decoupling process. In addition, we assessed the designability of different interfaces in Figure S29. Existing designs (Figure S29 (a-b)) often feature simple empirical or bioinspired geometries with limited control over interface anisotropic properties in a single direction. In contrast, the metainterface (Figure S29 (c)) consists of a minimum design unit, the single stinger, which orients itself to provide highly programmable and localized thermomechanical behaviors that were previously unattainable.

**Supplementary Note 2.** Effects of metainterfaces on composite metamaterials with bending-dominated and stretch-dominated lattice implants.

In bending-dominated composite metamaterials, there is a 3% (vintiles) to 11% (SHS) improvement in SEAs compared to their conventional counterparts, while stretch-dominated metamaterials exhibit a 9% (BCC) to 18% (FCC) improvement in SEAs, as shown in Figure 3 (c). Stretch-dominated lattices display higher stress-strain curves compared to bending-dominated structures, and the improvements in SEAs facilitated by metainterfaces are more pronounced. For example, the results of struct-based lattice topologies indicate that the SEA improvements in stretch-dominated lattices are 3 to 9 times higher than in bending-dominated lattices. In addition, an increase in the interface area introduces greater improvements in SEAs, as seen in the case of SHS filled with metainterfaces, which exhibit a 4-fold improvement in SEAs compared to vintiles.

These results provide valuable design guidelines, suggesting that metainterfaces with stiffer interface parent geometries and a larger interface contact area yield more significant mechanical advancements. Furthermore, it is evident that the truss elements of bending-dominated composite metamaterials (Figure S25) tend to fracture prematurely compared to the stretch-dominated lattices (Figure 4 (e)). This premature fracture results in an early separation of the matrix and reduced interface reactions, which in turn explains the observed early decline in the stress-strain curves in Figure S24 and the less pronounced improvements in SEAs in bending-dominated structures. Moreover, the occurrence of interfacial fractures underscores the findings that increasing the contact interface area equipped with metainterfaces leads to more effective enhancements in both SEAs and stress-strain curves. In addition, it is observed that the truss of the bending-dominated composite metamaterials exhibit an early fracture compared to the stretch-dominated lattices, leading to an early separation of the matrix and lower interface reactions. This explains the observed earlier decay of the stress-strain curves, and less effective improvements in SEAs of bending-dominated structures.

**Supplementary Note 3.** Case studies of active programming in amphibious robotic feet

To demonstrate the versatility of the metadisk, we have explored its potential application in amphibious robotic feet (Figure S26 (a)), which can exhibit programmable mechanical behaviors on land using the design principles described in equations (6-8), and achieve programmable flow control in water. By precisely controlling the concentration angle, this robotic foot can effectively concentrate and direct the flow to desired locations Figure S26 (b-c), achieving flow modulation ranging from 96% to 115% of the inlet flows as the concentrating angles vary from 0º to 60º (Figure S26 (d)). This illustrates the potential of employing metainterfaces in systems with programmable multifunctionalities, such as real-time controlled mechanical interface reactions and flow controls.

**Supplementary figures and tables**

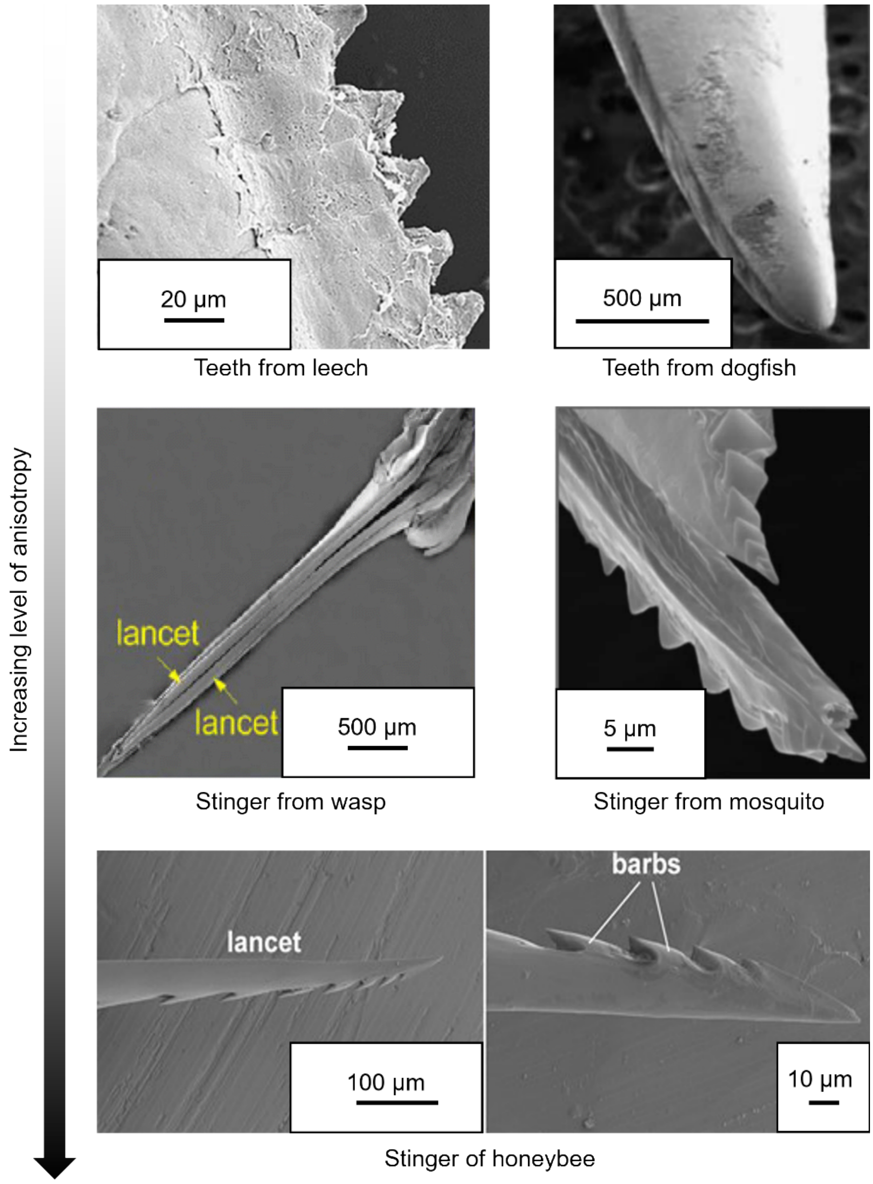


Figure S1. The sharp geometries of different species with increasing anisotropy including the teeth from leech [1], the teeth from dogfish [2], stinger from wasp [3], stinger from mosquito [2], and stinger with backward barbs from honeybee [8].

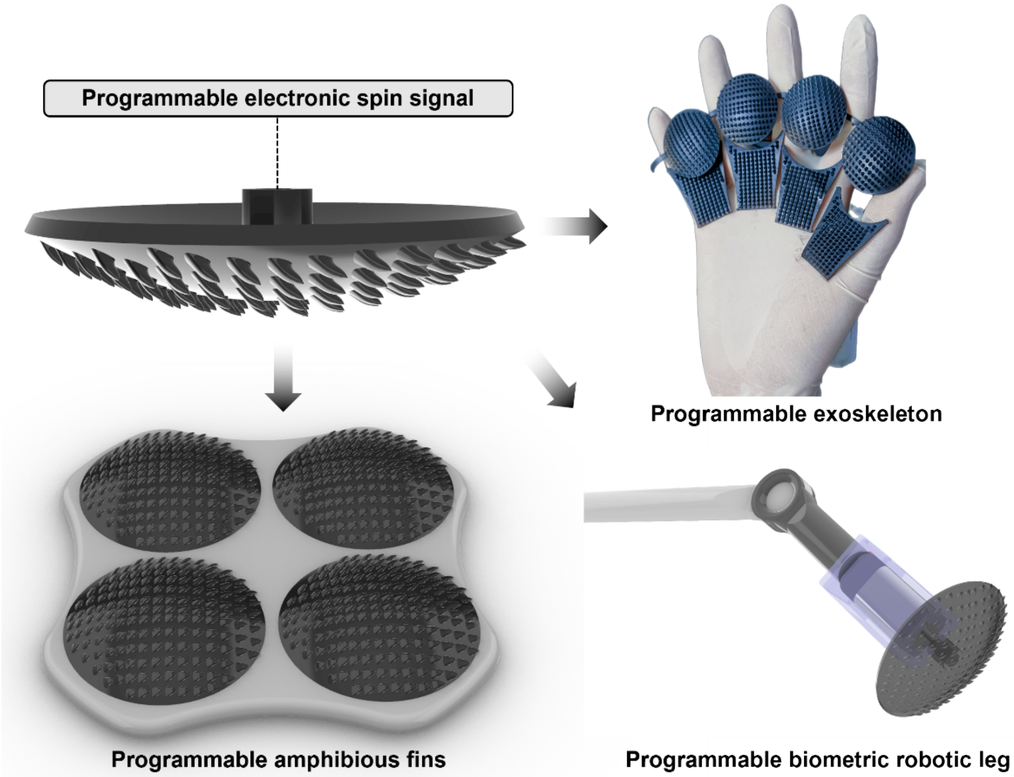


Figure S2. Potential applications of metadisk in various robotics systems.

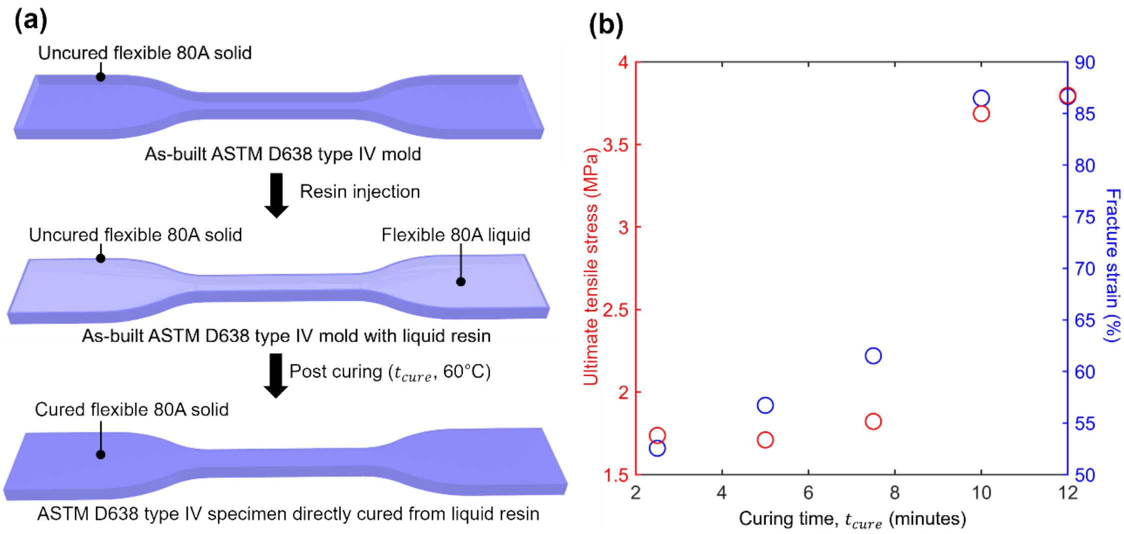


Figure S3. Experimental designs and testing of flexible 80A specimen directly cured from liquid. (a) Specimen preparation. (b) Results of the mechanical testing.

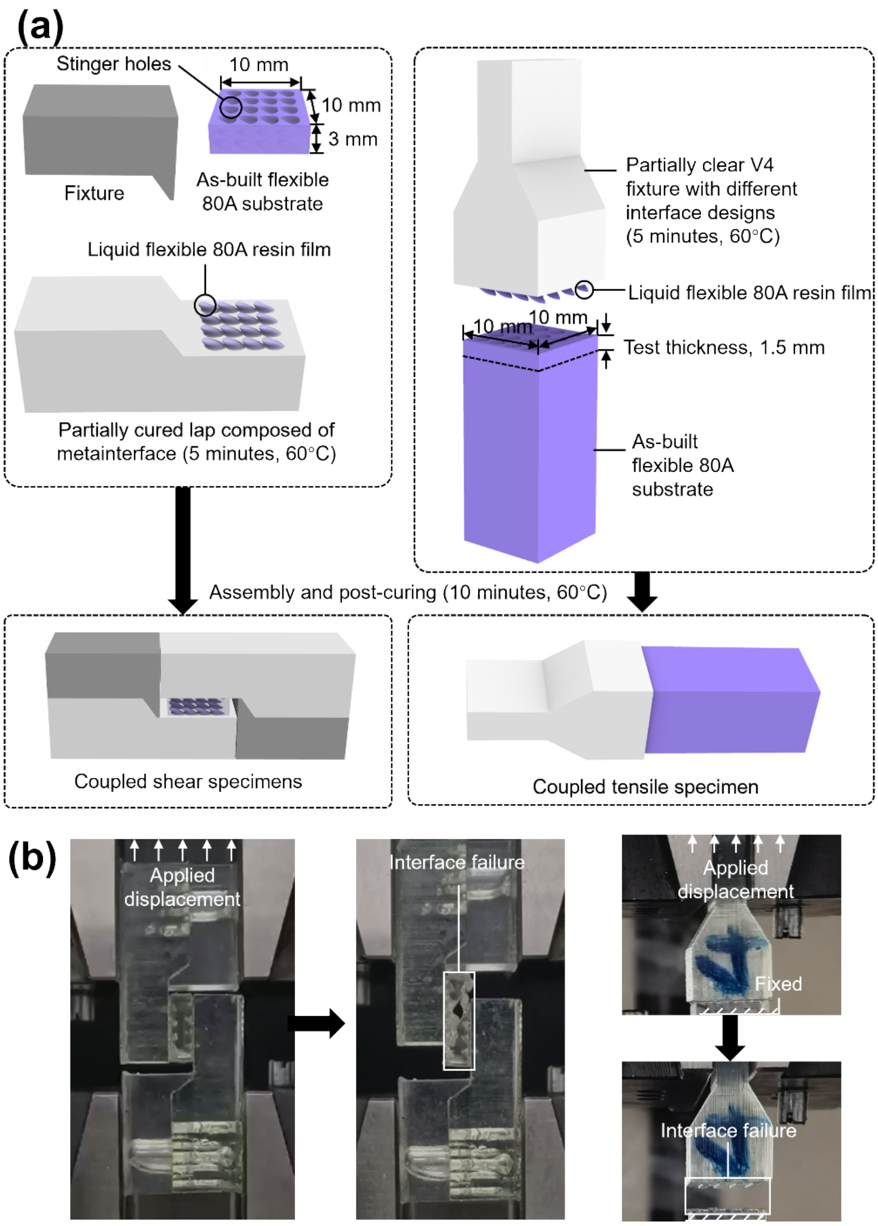


Figure S4. Designs and shear and tensile experiments for the measurement of coupled interface energies. (a) Design and preparation of specimens. (b) Experimental process.

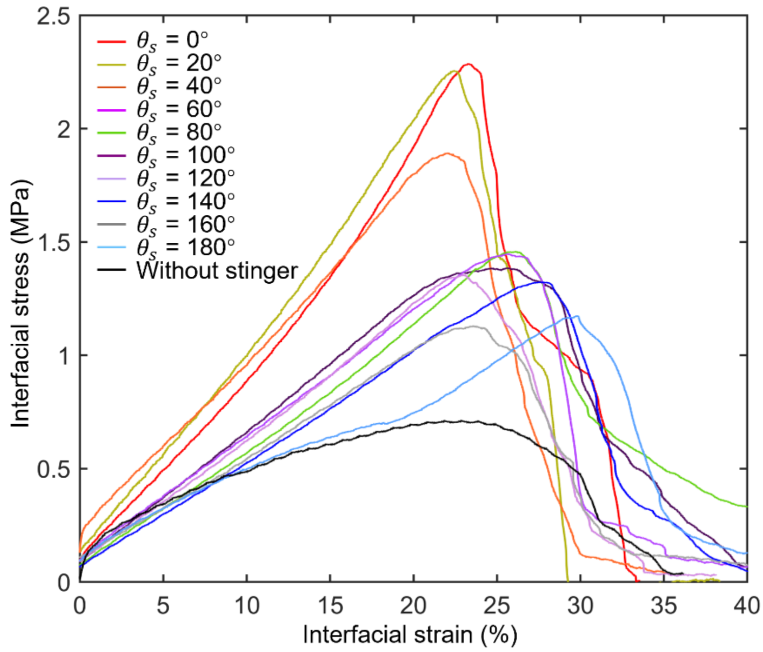


Figure S5. Stress-strain curves of the metainterfaces and interfaces without stingers under coupled stress condition.

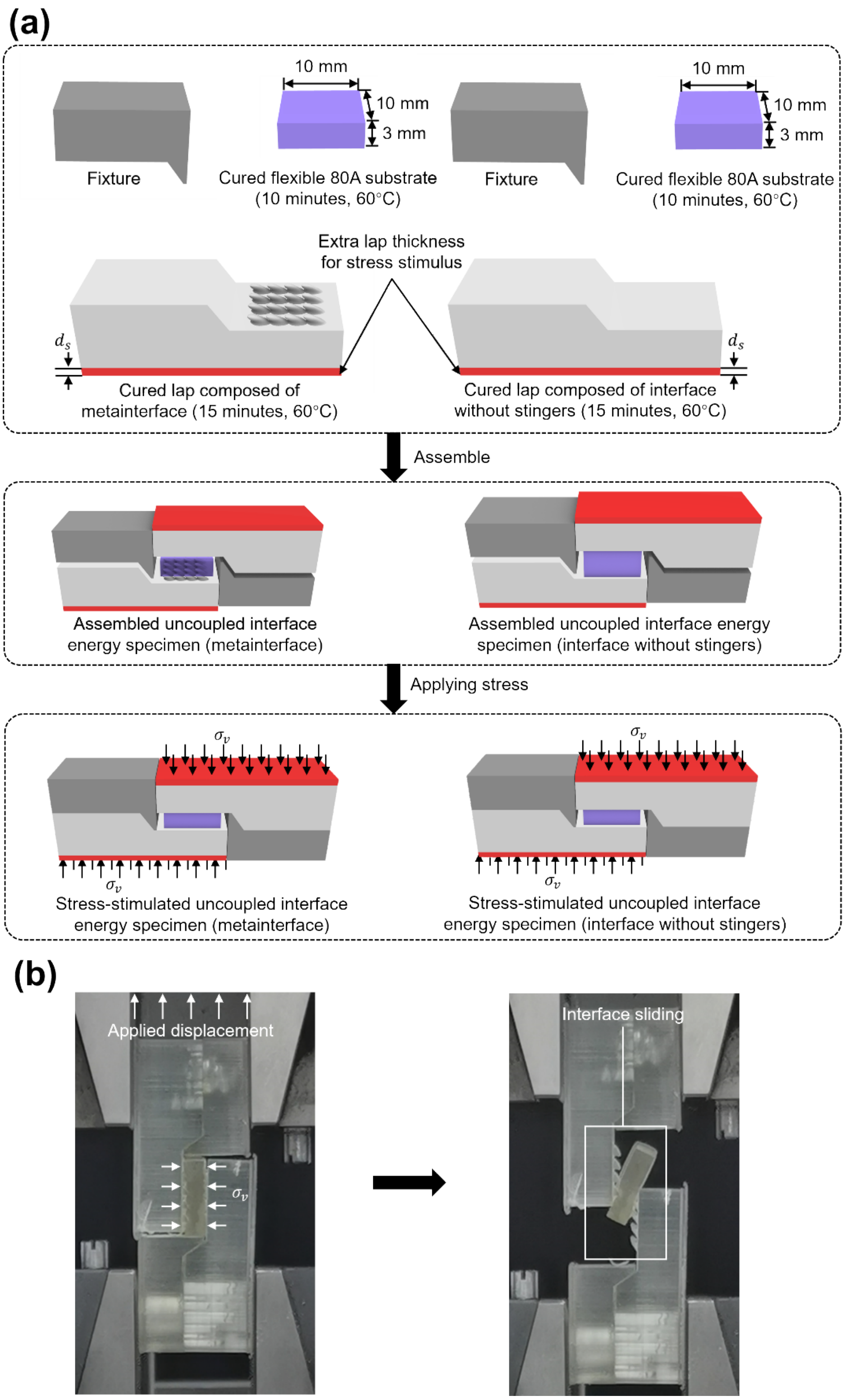


Figure S6. Designs and shear experiments for the measurement of uncoupled interface energies. (a) Design and preparation of specimens; and (b) Experimental process.

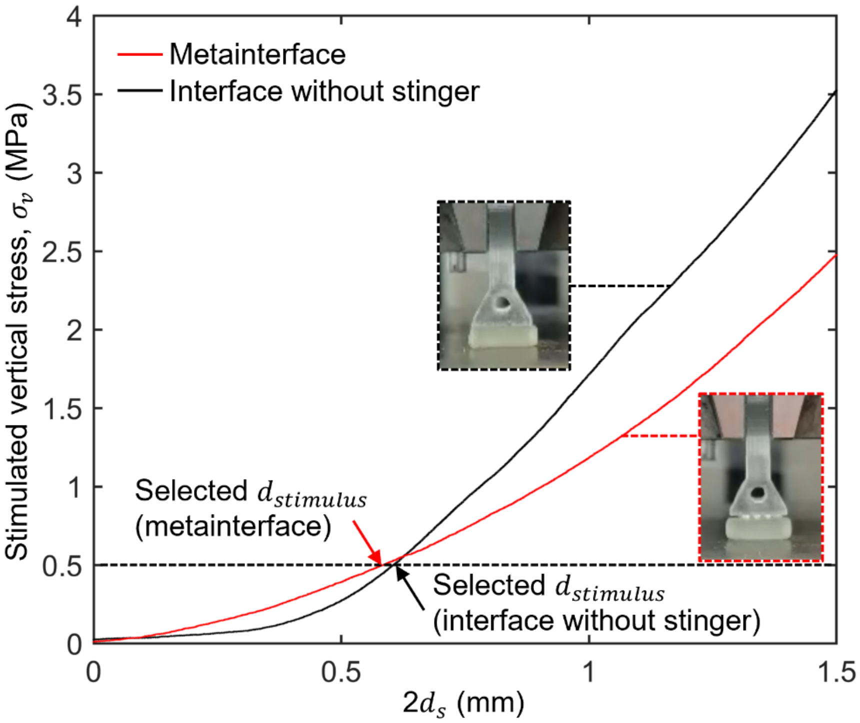


Figure S7. Stimulated vertical stress of the metainterfaces and interfaces without stingers under compression.

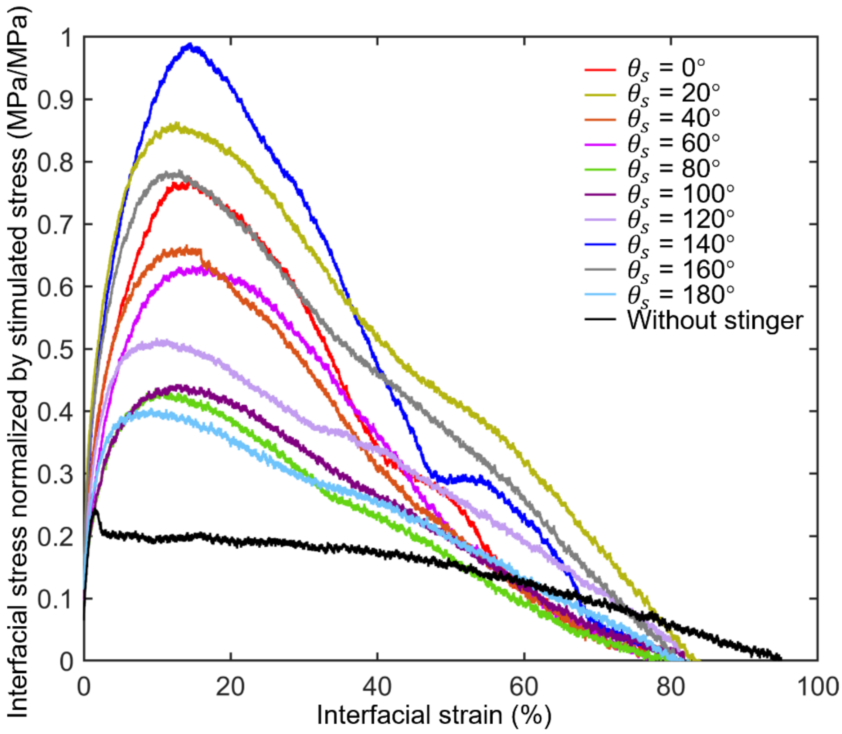


Figure S8. Stress-strain curves of the metainterfaces and interfaces without stingers under uncoupled stress condition.

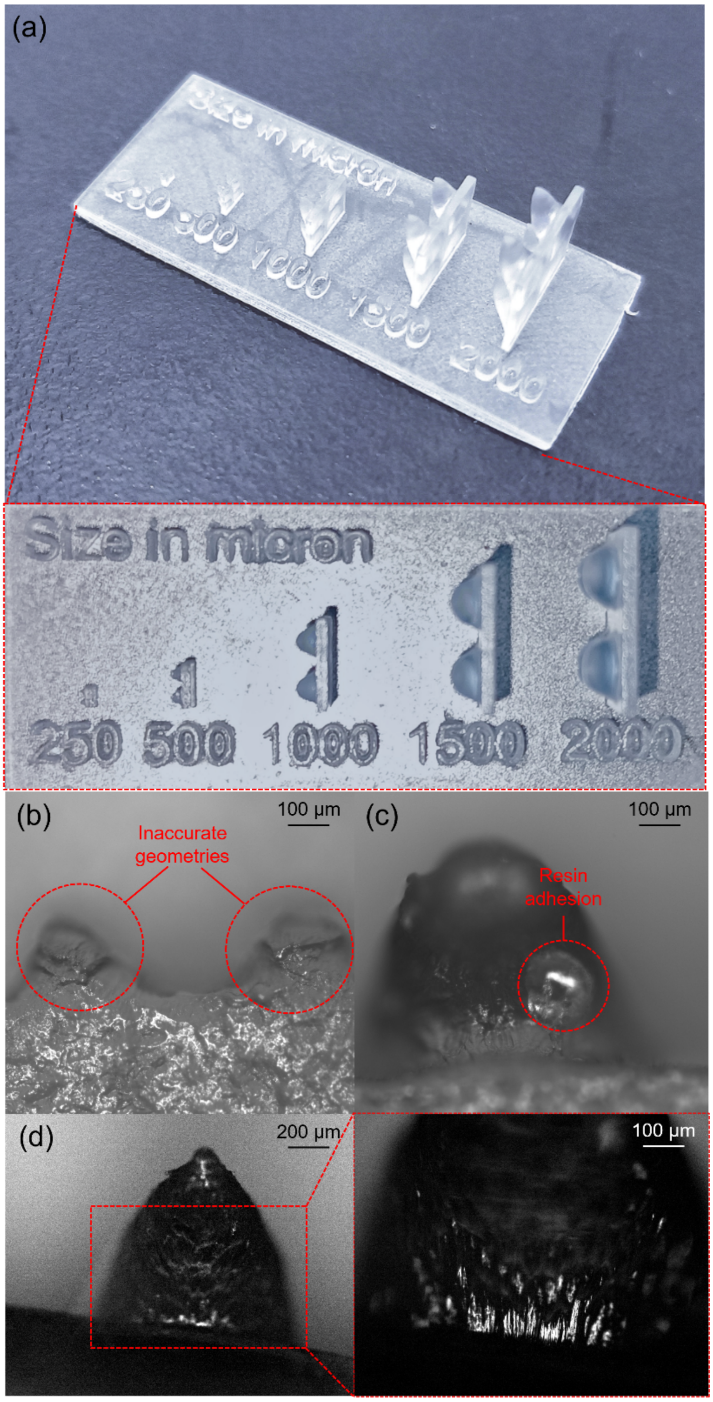


Figure S9. (a) The printed stingers with sizes ranging from 500 to 2000 µm. (b-d)The surface finishes captured by Zeiss AX10 optical microscope for the with 250 µm stingers, 500 µm stingers, 1000 µm stingers, respectively.

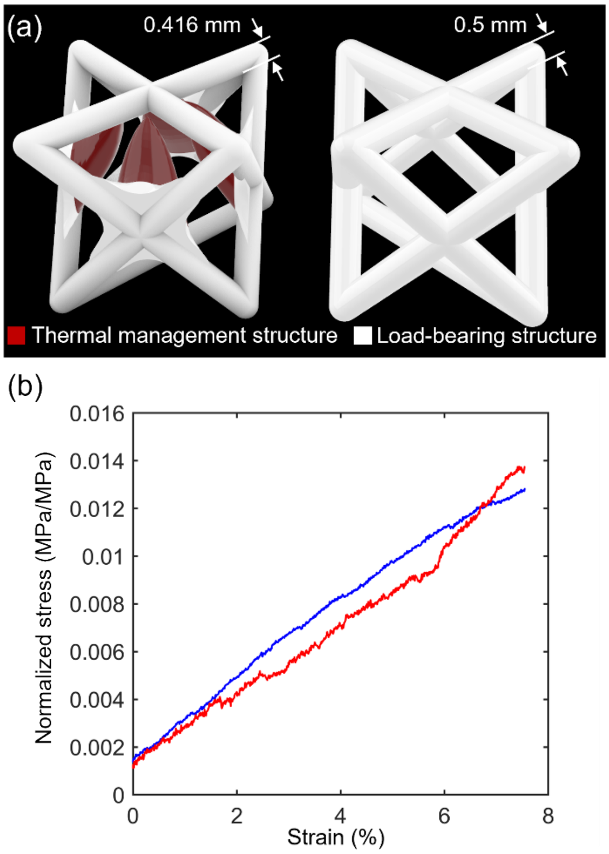


Figure S10. The (a) detailed design images and (b) the stress-strain curves normalized by the modulus of the parent material for the thermos-mechanical metamaterial and its conventional counterpart designed in this work.

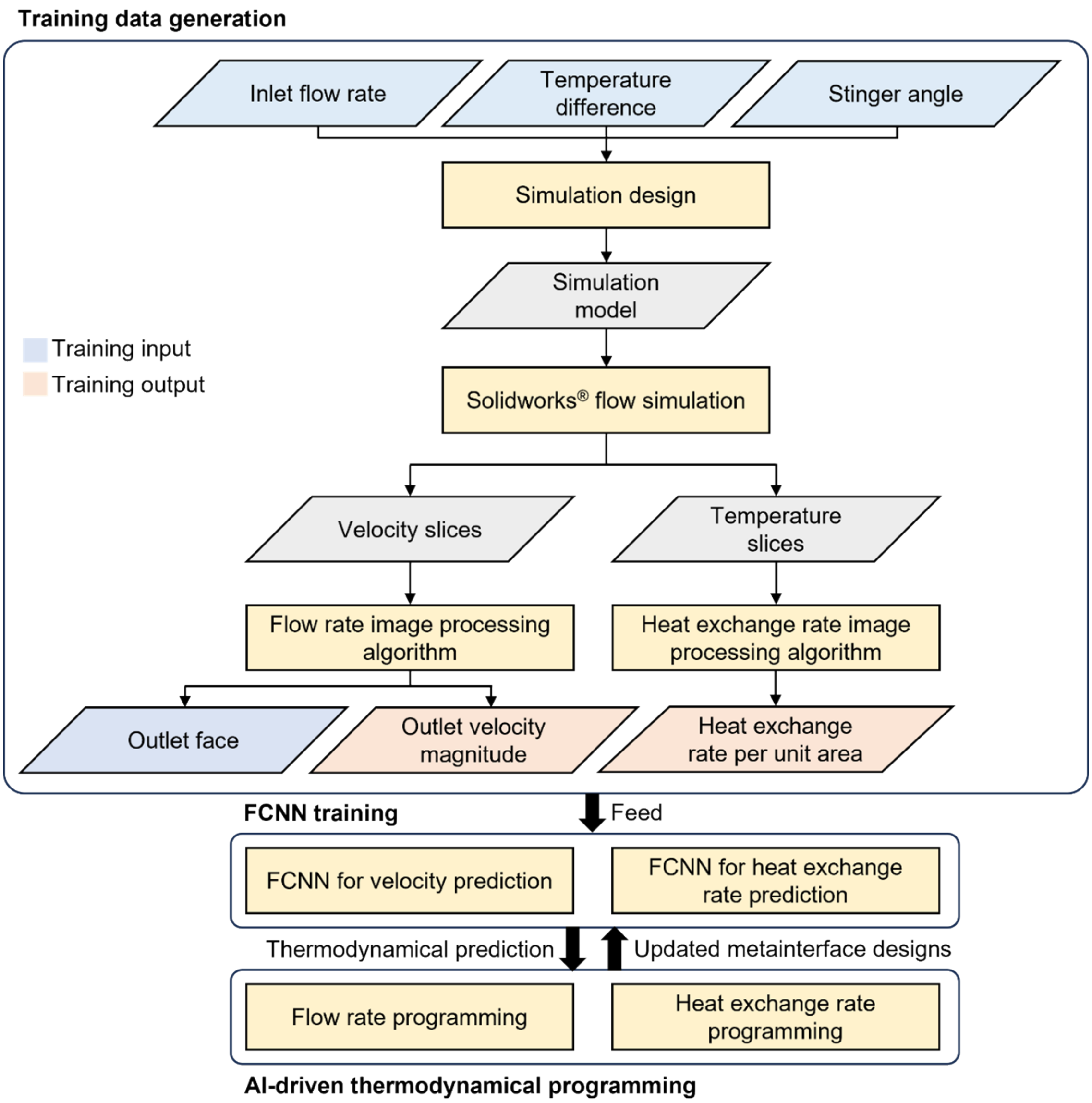


145
146 Figure S11. Flowcharts of machine learning process.

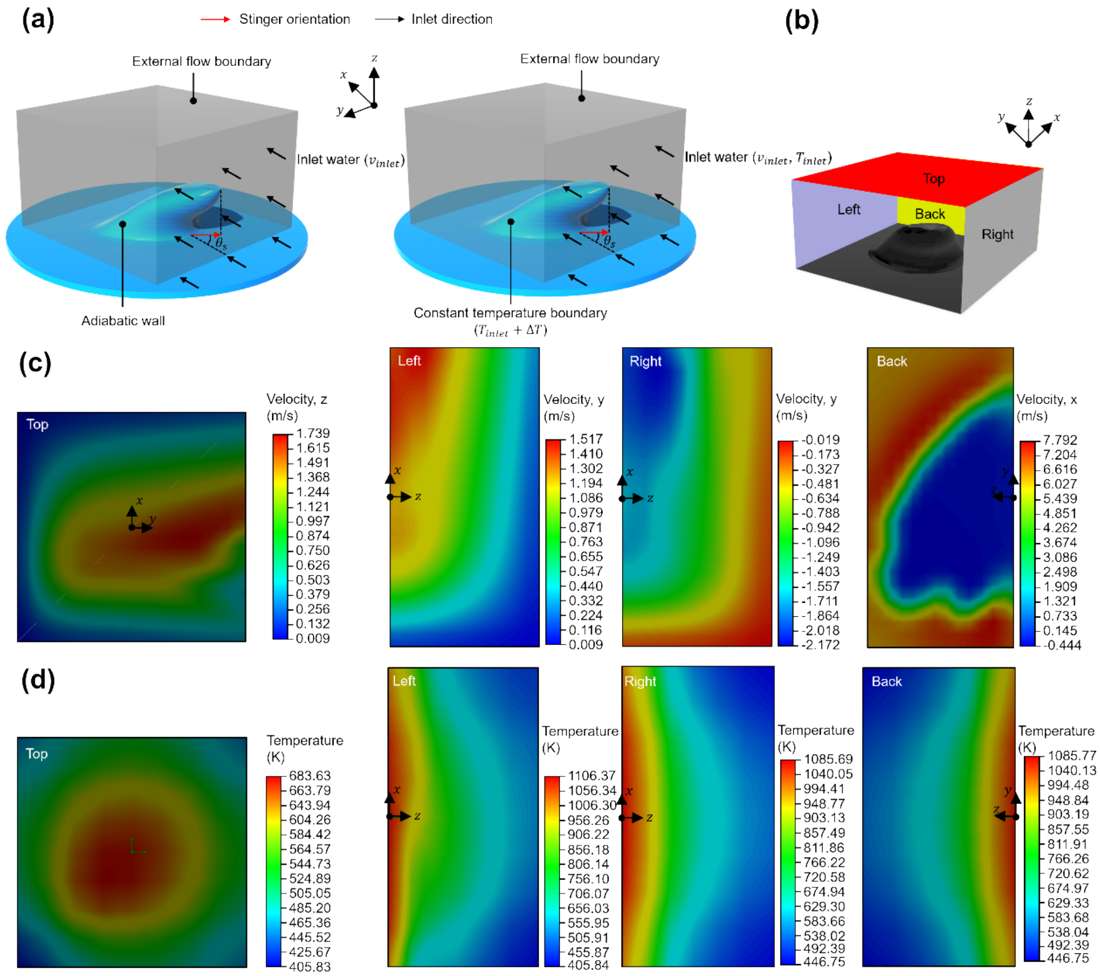


Figure S12. Configurations for thermodynamical simulations. (a) The computational domain and boundary condition of the simulation. (b) Different outlet faces of the simulation. (c) The training data slices for flow rate image processing algorithm. (d) The training data slices for heat exchange rate image processing algorithm.

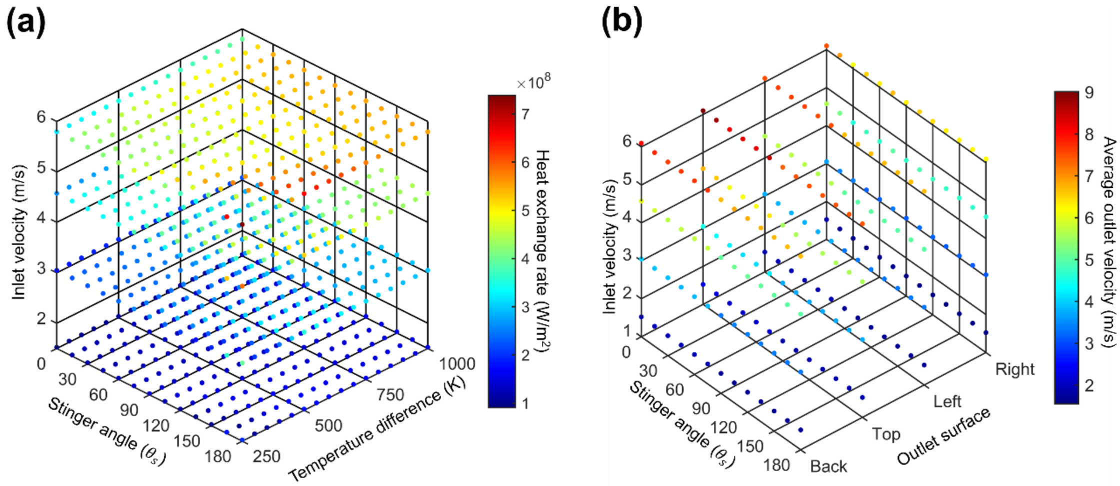


Figure S13. Training data distribution. (a) The heat exchange rate outputs with different training inputs. (b) The velocity outputs with different training inputs.

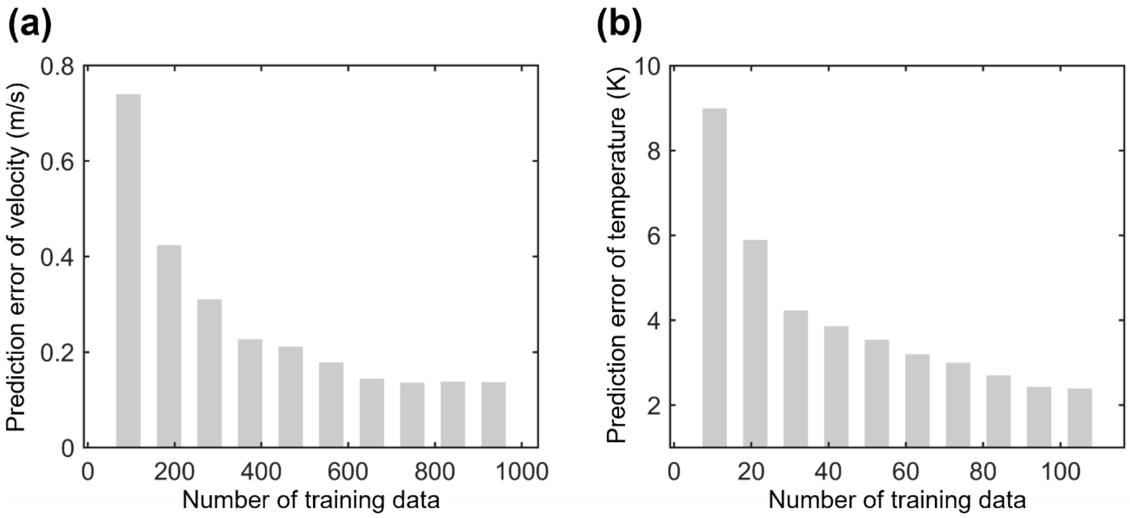


Figure S14. Prediction test errors reduces as the number of training data increases for predicting (a) velocity, and (b) temperature.

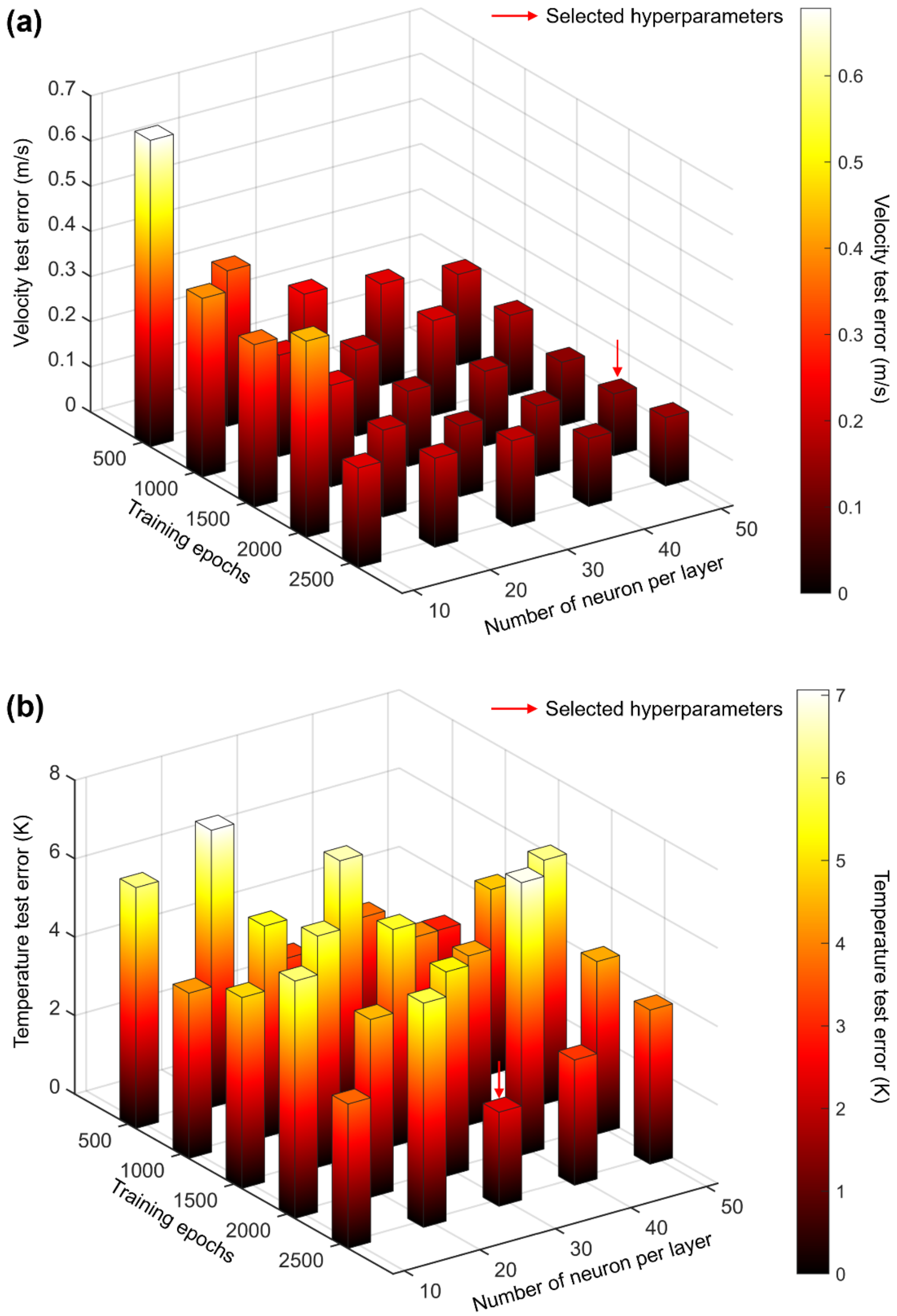


Figure S15. Prediction test errors for differrent hyperparameters of the FCNNs to predict (a) velocity, and (b) temperature.

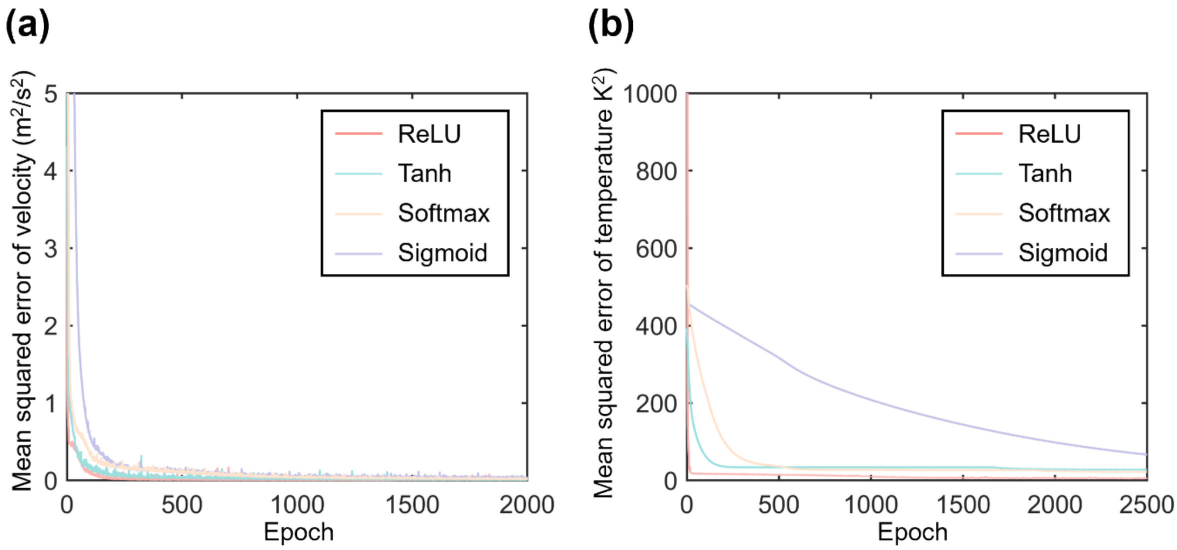


Figure S16. The training loss comparing different activation functions for the FCNNs predicting (a) velocity and (b) temperature.

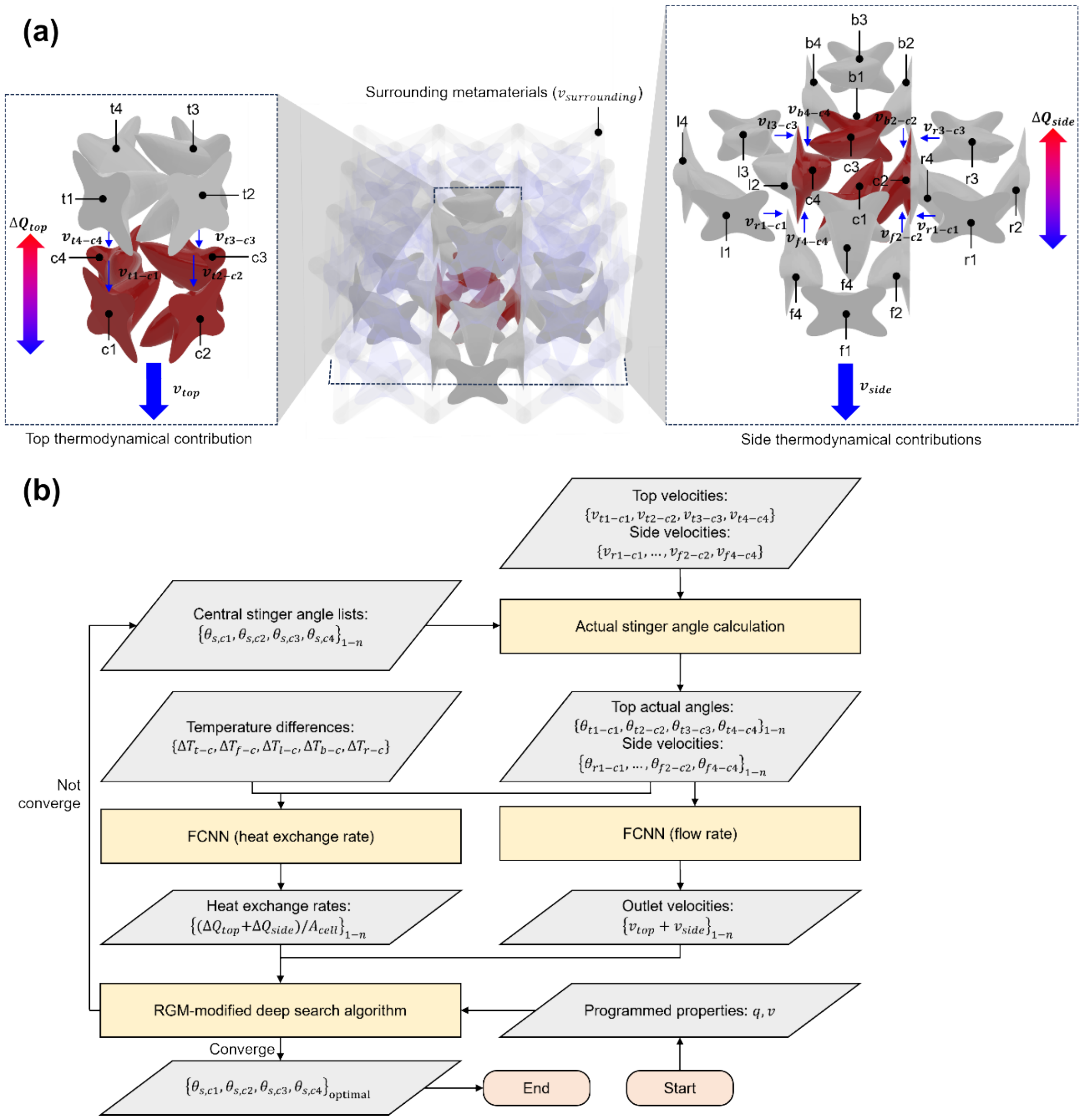


Figure S17. The thermodynamical programming algorithms. (a) Theoretical flow rate and heat exchange rate design schematics and (b) flow charts of programming the flow rate and heat exchange rate. Note that $\theta_{s,X}$ represents the stinger angle of the stinger $X$, $v_{X-Y}$ is the flow rate from stinger $X$ to stinger $Y$, $\theta_{X-Y}$ represents the angle between the velocity $v_{X-Y}$ and stinger $Y$, $\Delta T_{R1-R2}$ represents the temperature difference between the regions $R1$ and $R2$, $n$ is the batch size of the RGM-modified deep search algorithm, $v_{surrounding}$ is the negative flow contribution caused by the surrounding structures of the metamaterials, $A_{cell}$ represents the area of a unit cells implanted with four stingers, $\Delta Q_{top}$ and $\Delta Q_{side}$ represent the total heat exchanged from the top flows and the side flows, respectively, $v_{top}$ and $v_{side}$ are the outlet flow rates from the top flows and the side flows, respectively, $q$ and $v$ represent the desired heat exchange rate and the outlet velocity, respectively.

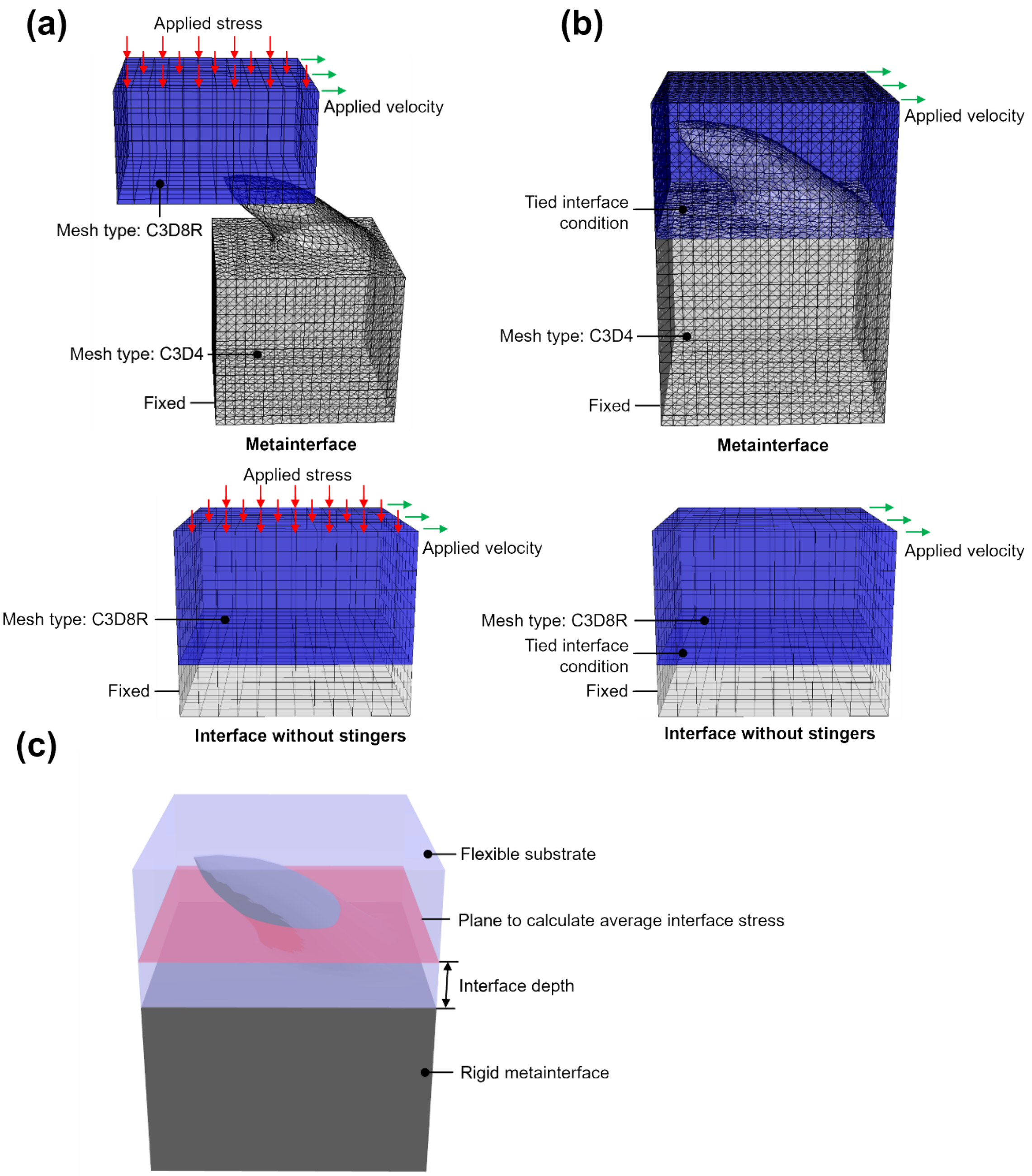


Figure S18. The simulation configuration to calculate the interface stresses of metainterfaces and interfaces without stingers. (a) Uncoupled stress conditions. (b) Coupled stress conditions. (c) The definition of the interface depth and the corresponding plane for interface stress average calculations.

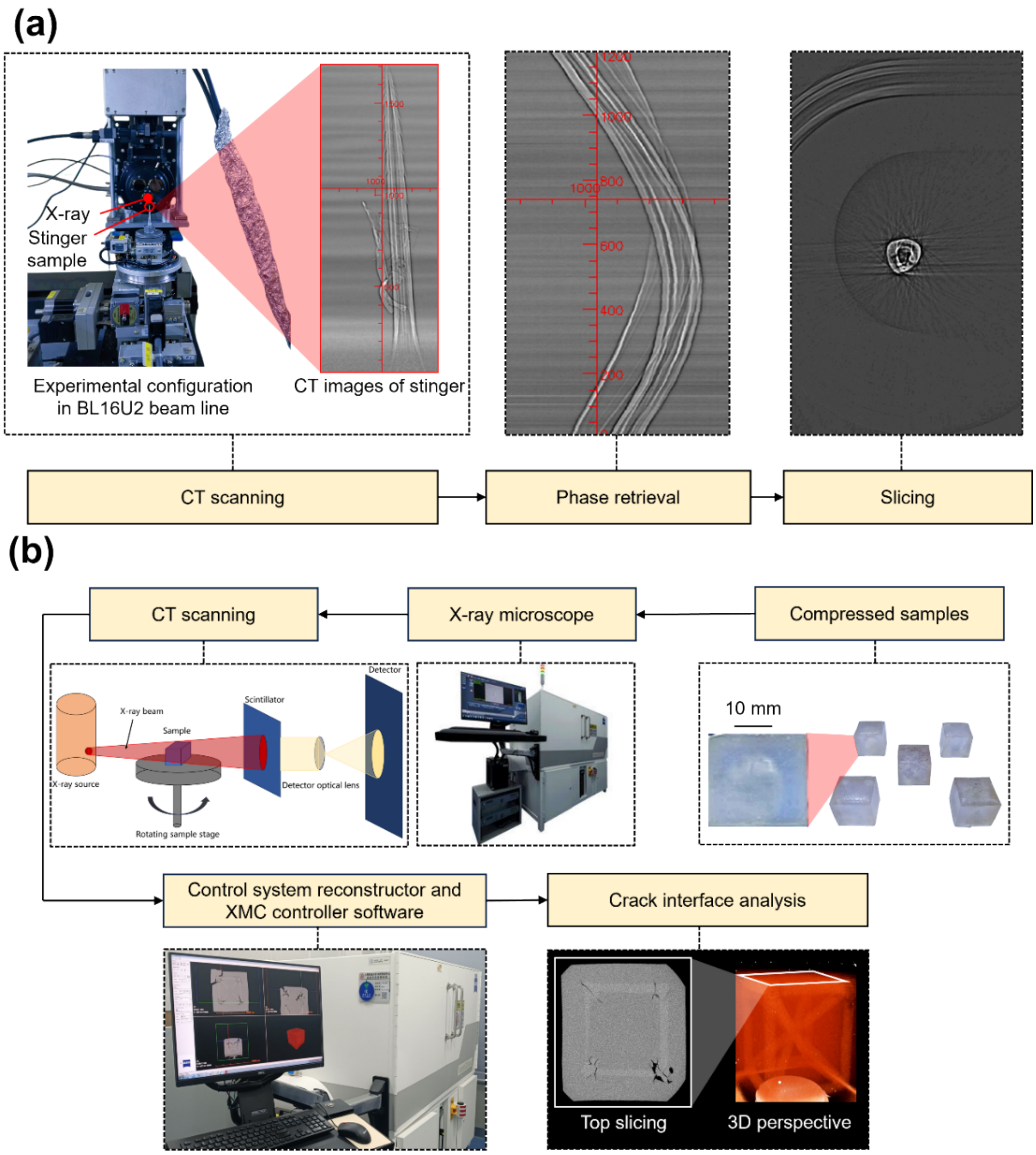


Figure S19. The XCT experiments. (a) Flow chart of XCT experiments using the BL18B beamline of Shanghai Synchrotron Radiation Facility (SSRF). (b) Flow chart of XCT experiments using the ZEISS Xradia 520 Versa X-ray microscope at Instrumental Analysis Center of Shanghai Jiao Tong University (SJTU).

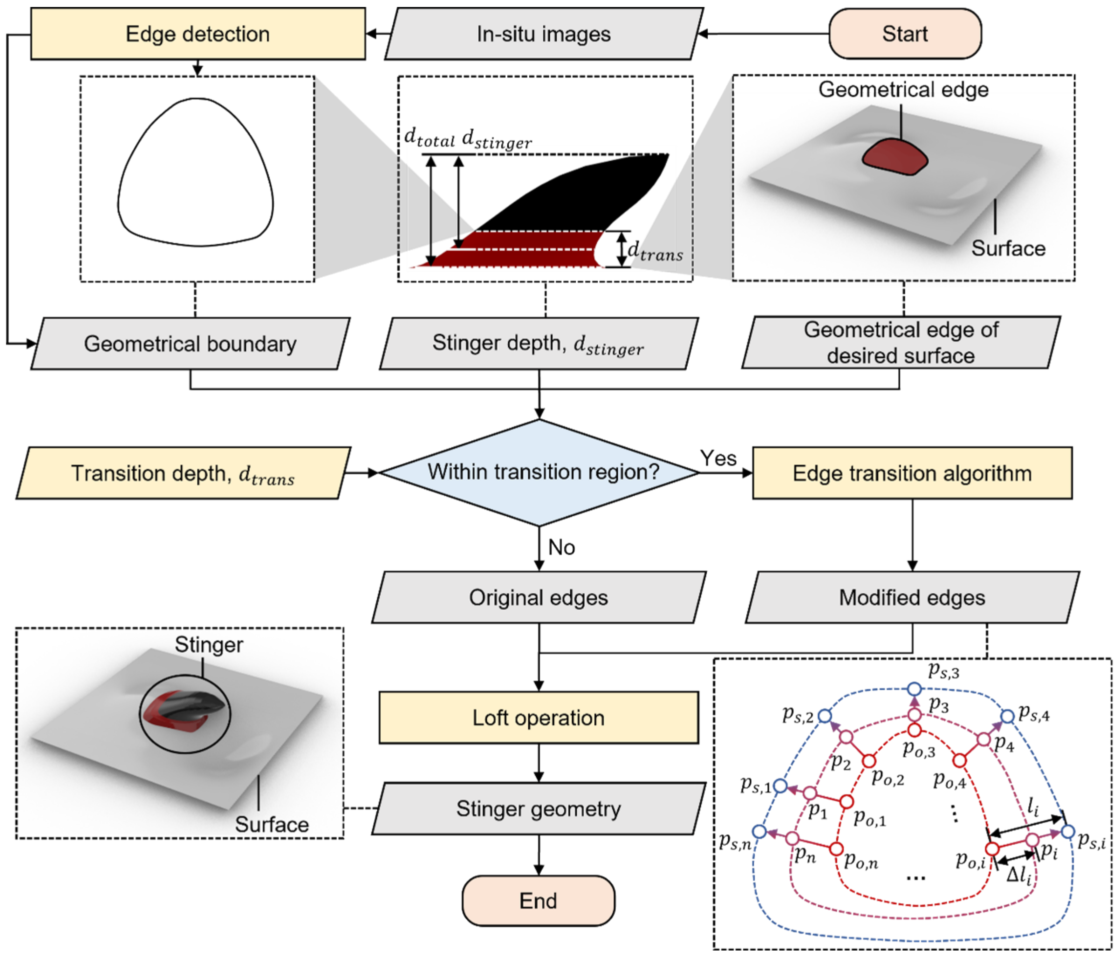


Figure S20. The re-construction of stinger geometries based on the XCT results on a freeform geometry.

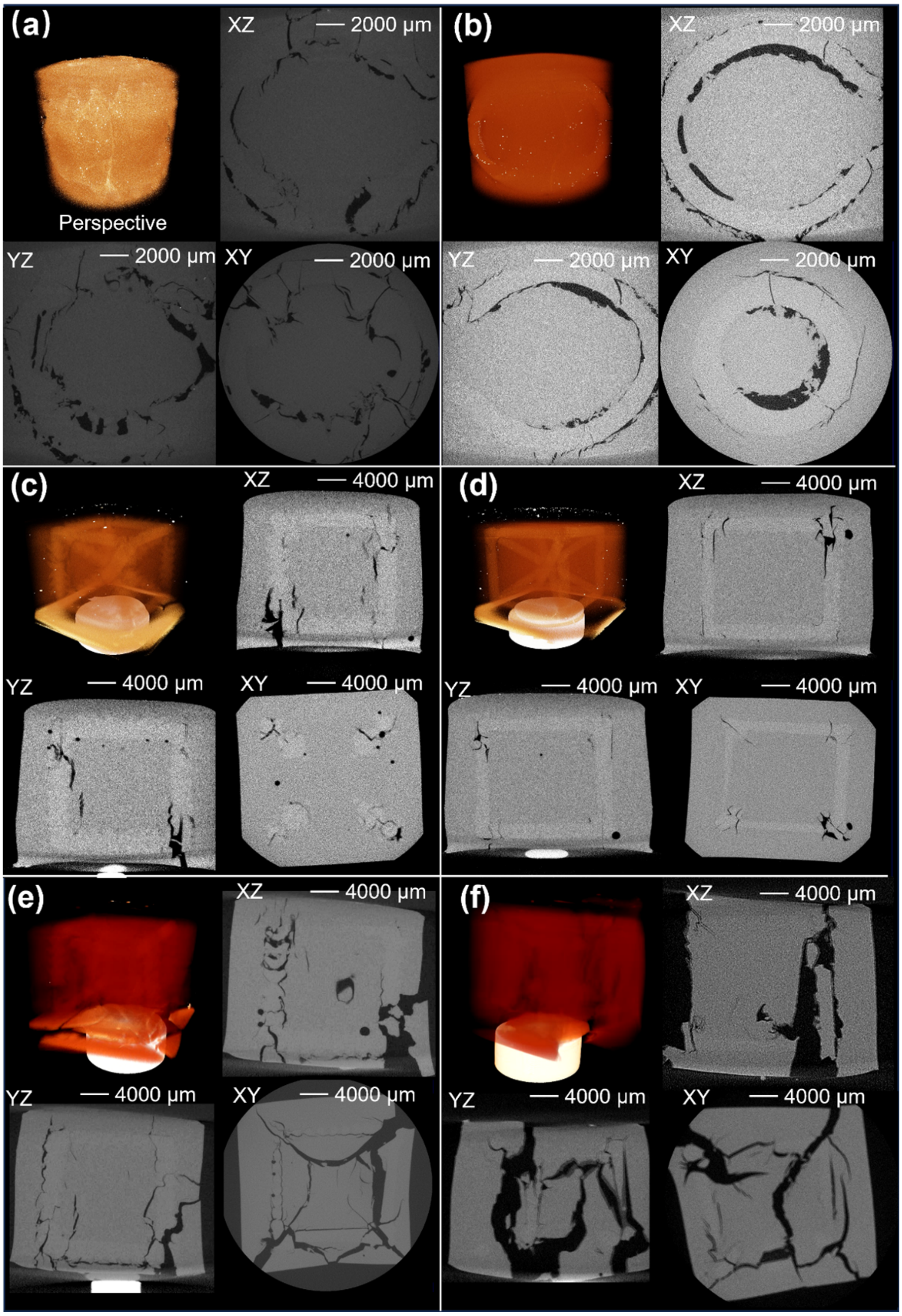


Figure S21. XCT images of internal interface fractures. (a) Spherical hollow structures (SHS) metamaterials with metainterfaces. (b) SHS metamaterials with conventional interfaces. (c) Body-centered-cubic (BCC) metamaterials with metainterfaces. (d) BCC metamaterials with conventional interfaces. (e) Tesseract metamaterials with conventional interfaces. (F) Tesseract metamaterials with conventional interfaces.

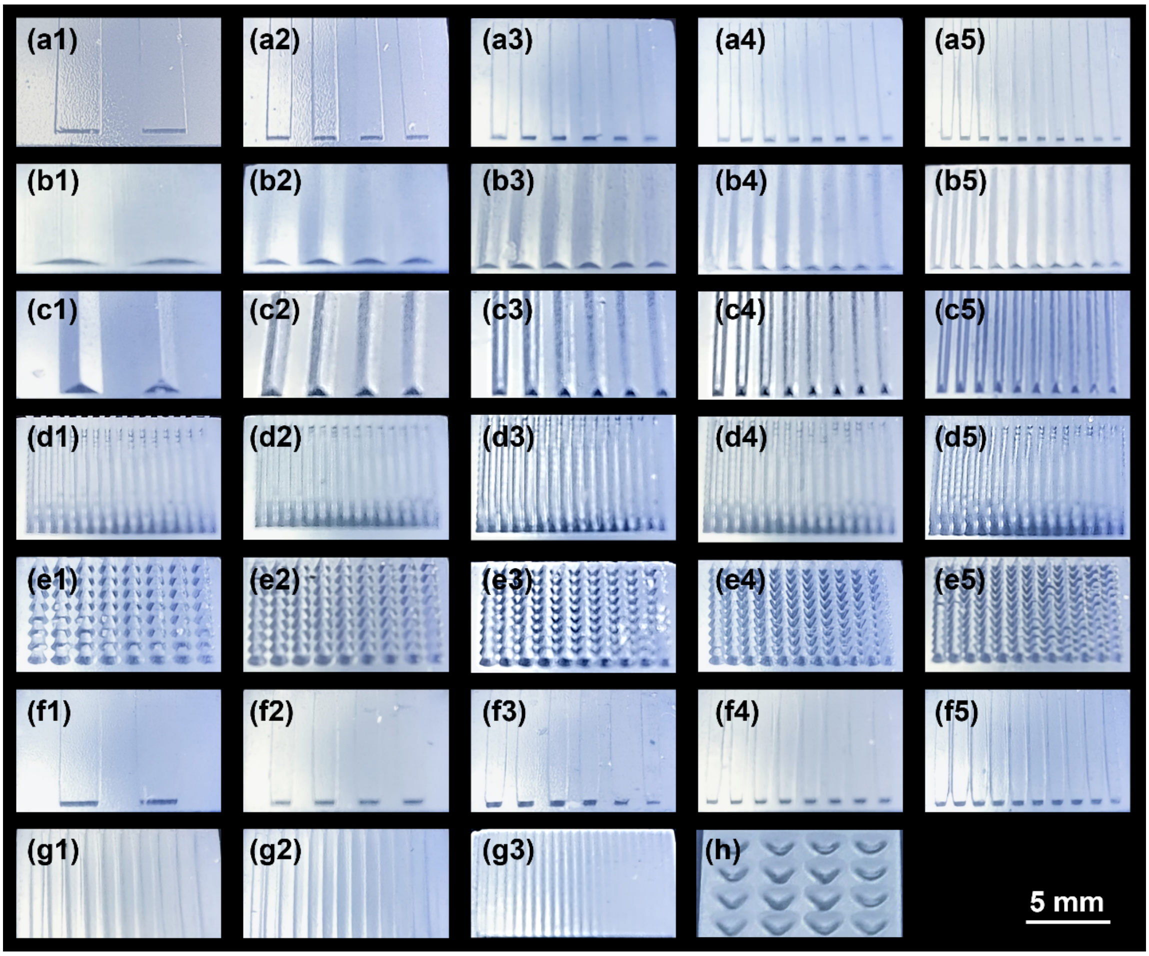


Figure S22. Interface modifications included in this study. (a1-a5) The conventional interface modifications with rectangular shapes. (b1-b5) The conventional interface modifications with wavy shapes. (c1-c5) The conventional interface modifications with traingular shapes. (d1-d5) The biometric interface modifications inspired by stinger from honeybee. (e1-e5) The biometric interface modifications inspired by stinger from parasite. (f1-f5) The trapezium biometric interface modifications inspired by elytra of beetle. (g1-g3) The ellipse biometric interface modifications inspired by elytra of beetle. (h) The metainterface designed with XCT-rebuild stinger geometry of honeybee.

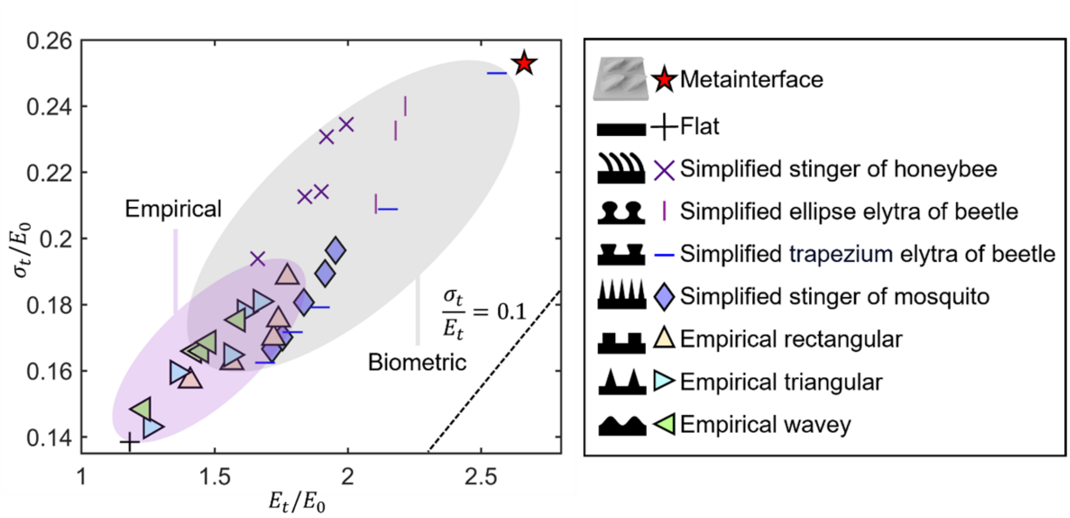


Figure S23. Ashby chart comparing the Tensile strength $\sigma_t$ and tensile modulus $E_s$ for different interfaces normalized by the modulus of parent material $E_0$ of metainterfaces and existing interface designs including the flat interface, interface modified by empirical conventional rectangular, traingular, and wave shapes [9], inspired by stingers of honeybee [10] and parasite [11], and elytra of beetle with trapezium [12] or ellipse [13] simplifications. Note that the pentagon represents the metainterface with highest tensile strength and modulus.

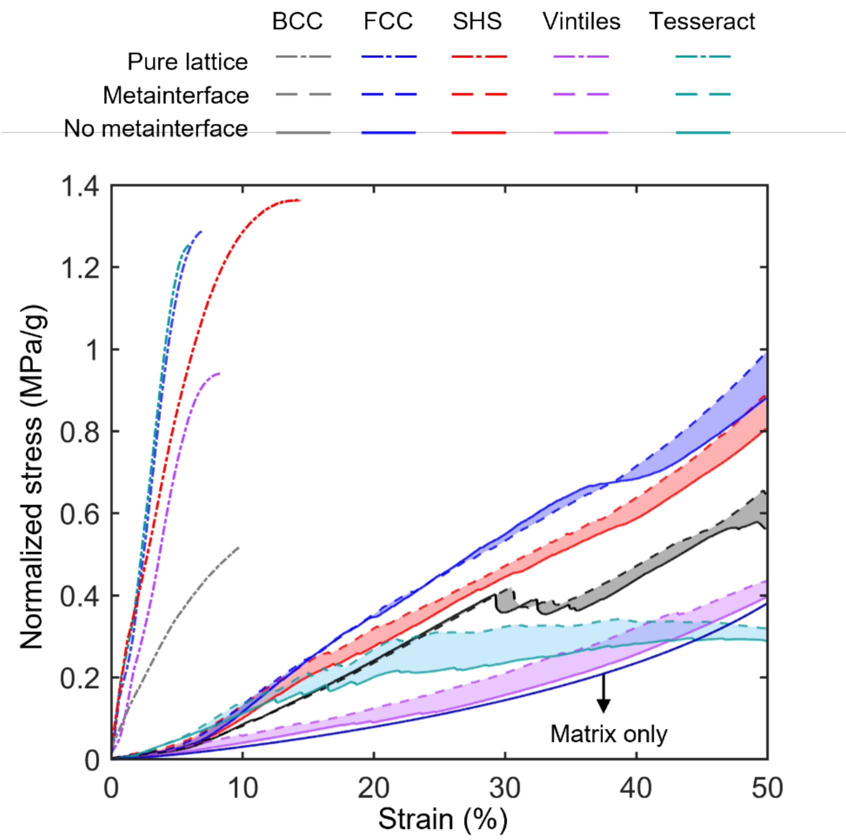


Figure S24. The normalized compressive stress-strain curves of pure lattice structures fabricated with clear V4 resin, pure matrix materials prepared with flexible 80A resin, composite metamaterials with and without programmed metainterfaces.

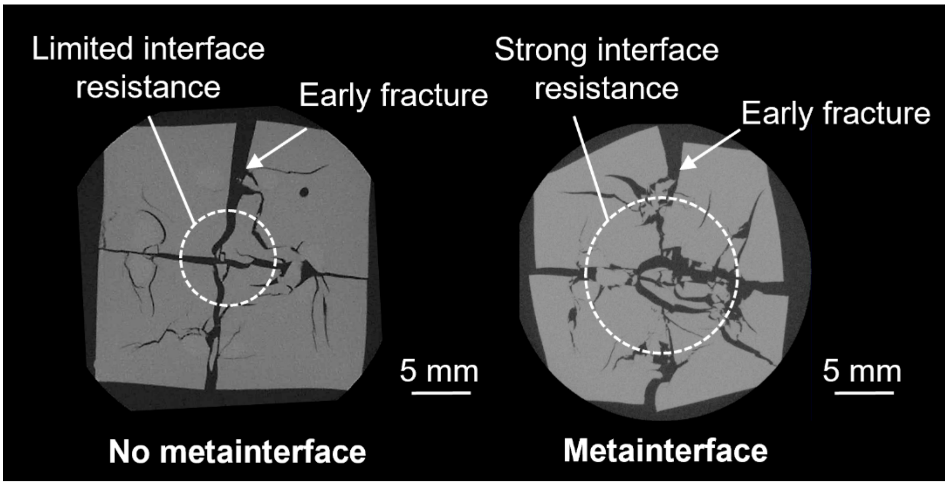

Figure S25. The interface cracks for bending-dominated vintiles composite metamaterials with and without programmed metainterfaces.

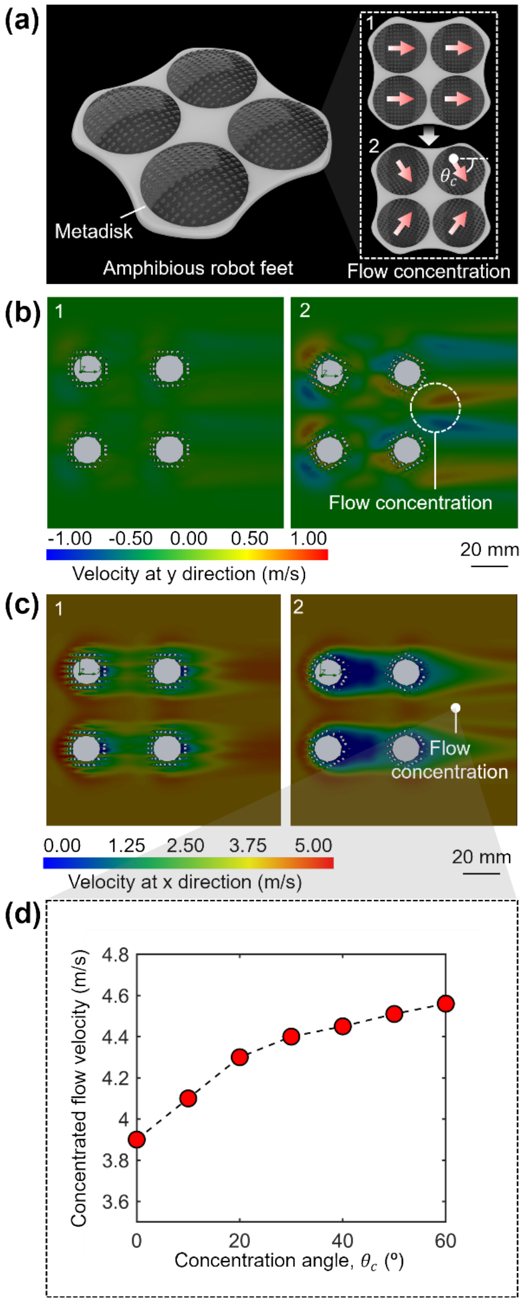


Figure S26. (a) Amphibious robot feet with programmable uncoupled mechanical and thermodynamical behaviors, where the inlet flow rate is set to 4 m/s, $\theta_c$ is the flow concentrating angle. (b-c) Flow velocity distributions at y and x direction, respectively, of the amphibious robot feet with $\theta_c = 0^{\circ}$ and $\theta_c = 60^{\circ}$. (d) Programmable concentrated flow velocity for different $\theta_c$.

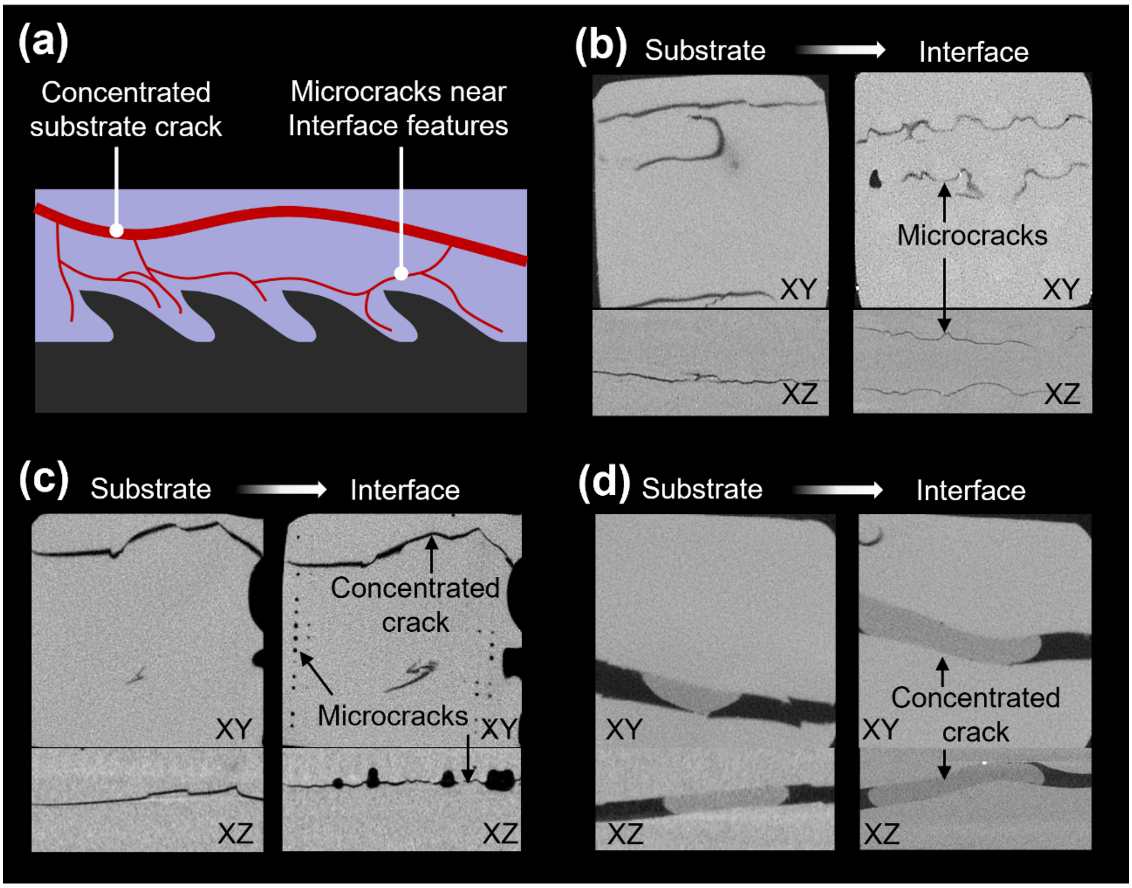


Figure S27. The (a) theoretical crack distribution diagram and XCT-scanned crack extensions from the substrate to the interface design regions for (b) metainterface with XCT-rebuild biostructure, (c) interface inspired by honeybee-stinger, and (d) interface inspired by elytra of beetle.

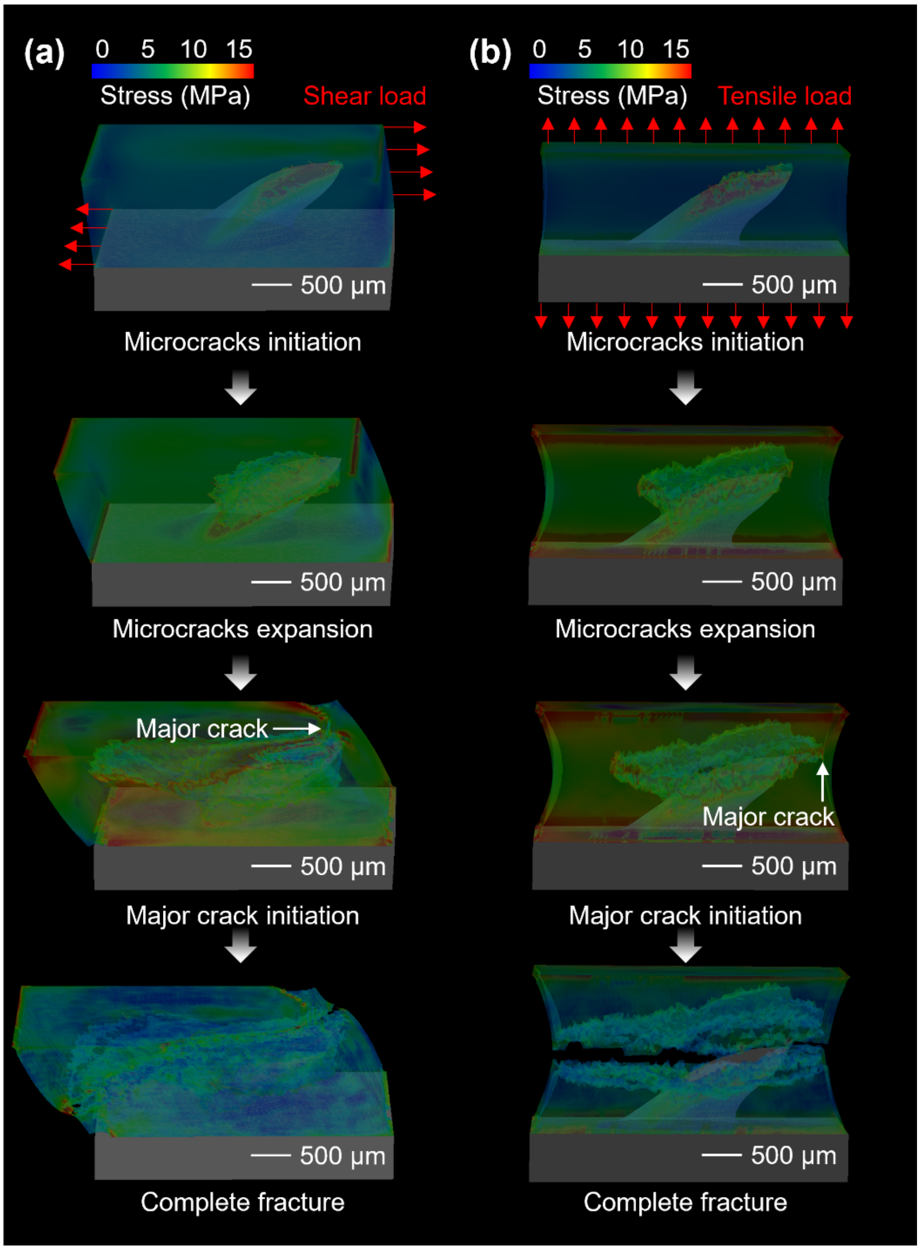


Figure S28. Simulated fracture process of metainterface under (a) shear and (b) tensile load conditions.

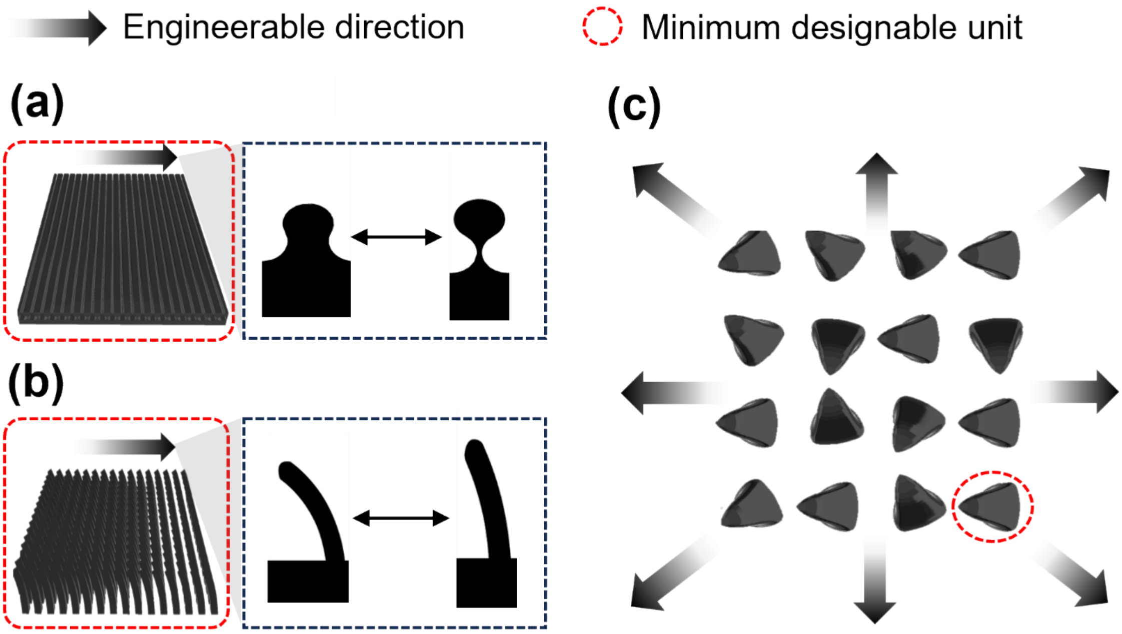


Figure S29. Schematic diagrams of the interface directional designability for (a) interfaces with conventional modifications or inspired by elytra of beetle, (b) interfaces inspired by stinger of honeybee, and (c) metainterfaces.

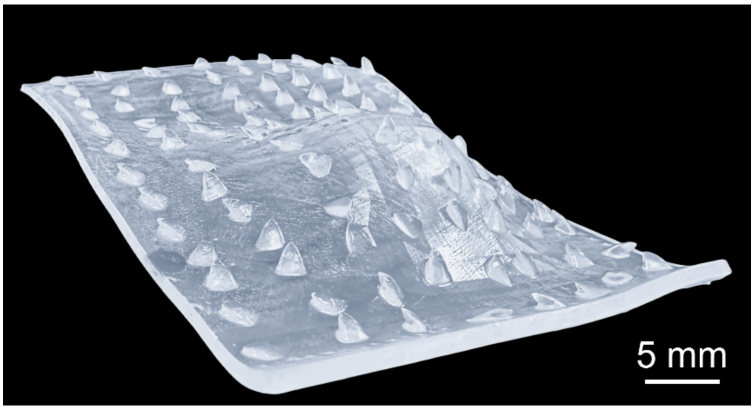

Figure S30. Fabricated freeform metainterface.

Table S1. The post-processing conditions of the parent materials for different types of experiment.

| Experiment | Initial form | Curing time (minutes) | Curing temperature (°C) |
|---|---|---|---|
| Basic mechanical properties of parent materials (standard clear) | Printed solids | 15 | 60 |
| Basic mechanical properties of parent materials (flexible 80A) | Printed solids or liquid | 2.5-12 | 60 |
| Metainterfaces and conventional interfaces for the measurement of coupled interface energy (standard clear) | Printed solids | 5 | 60 |
| Metainterfaces and conventional interfaces for the measurement of uncoupled interface energy (standard clear) | Printed solids | 15 | 60 |
| Substrates of metainterface for the measurement of coupled interface energy (flexible 80A) | Printed solids with adhered liquid | 10 | 60 |
| Substrates of metainterface for the measurement of uncoupled interface energy (flexible 80A) | Printed solids | 10 | 60 |
| Vertical stress measurement (standard clear) | Printed solids | 15 | 60 |
| Vertical stress measurement (flexible 80A) | Printed solids | 10 | 60 |
| Metainterfaces and conventional interfaces of composite metamaterials (standard clear) | Printed solids | 3 | 60 |
| Metainterfaces and conventional interfaces of composite metastructures (standard clear) | Printed solids | 15 | 60 |
| Substrates of composite metamaterials (flexible 80A) | Liquid | 12 | 60 |
| Substrates of composite metastructures (flexible 80A) | Printed solids | 10 | 60 |

Table S2. Mechanical properties of parent materials.

| Specimen type | Modulus (MPa) | Ultimate tensile stress (MPa) | Fracture strain (%) |
|---|---|---|---|
| Specimen 1 (flexible 80A) | 4.45 | 3.80 | 85.49 |
| Specimen 2 (flexible 80A) | 4.41 | 3.76 | 87.07 |
| Specimen 3 (flexible 80A) | 4.47 | 3.81 | 84.93 |
| Specimens (liquid cured flexible 80A) | 3.13 - 4.39 | 1.66 - 3.79 | 53.80 - 86.75 |
| Specimen 1 (standard clear) | 1662.52 | 48.97 | 8.36 |
| Specimen 2 (standard clear) | 1655.43 | 46.35 | 9.15 |
| Specimen 3 (standard clear) | 1669.34 | 50.23 | 7.97 |

Table S3. Summary of weights for the components of composite metamaterials.

| Topology | Diameter or thickness of samples (mm) | Interface type | Struct diameter (mm) | Relative density (%) | Assembly type | Weight (g) |
|---|---|---|---|---|---|---|
| BCC | 2 | Without metainterface | 1.00 | 6.44 | With flexible matrix | 13.51 |
| | | | | | Without flexible matrix | 0.87 |
| | | With metainterface | 0.84 | 6.62 | With flexible matrix | 13.45 |
| | | | | | Without flexible matrix | 0.89 |
| FCC | 2 | Without metainterface | 1.00 | 9.57 | With flexible matrix | 13.38 |
| | | | | | Without flexible matrix | 1.28 |
| | | With metainterface | 0.91 | 9.53 | With flexible matrix | 13.74 |
| | | | | | Without flexible matrix | 1.31 |
| SHS | 1 | Without metainterface | 1.00 | 4.33 | With flexible matrix | 13.62 |
| | | | | | Without flexible matrix | 0.59 |
| | | With metainterface | 0.85 | 4.24 | With flexible matrix | 13.43 |
| | | | | | Without flexible matrix | 0.57 |
| Vintiles | 2 | Without metainterface | 1.00 | 4.17 | With flexible matrix | 13.44 |
| | | | | | Without flexible matrix | 0.56 |
| | | With metainterface | 0.93 | 4.42 | With flexible matrix | 13.34 |
| | | | | | Without flexible matrix | 0.59 |
| Tesseract | 2 | Without metainterface | 1.00 | 7.01 | With flexible matrix | 13.70 |
| | | | | | Without flexible matrix | 0.96 |
| | | With metainterface | 0.88 | 7.10 | With flexible matrix | 13.10 |
| | | | | | Without flexible matrix | 0.93 |
| NA | NA | NA | NA | NA | Pure matrix | 13.47 |

Table S4. Summary of weights for the components of composite metastructures.

| Type of composite metastructures | Thickness design of each rigid sheet (mm) | Average weight of each rigid sheet (g) | Thickness design of flexible matrix between the sheets (mm) | Average weight of flexible matrix (g) | Density ($g/cm^3$) | Sheet-to-matrix volume ratio (%) |
|---|---|---|---|---|---|---|
| Composite metastructure without metainterfaces | 1 | 0.49 | 3.5 | 13.65 | 1.1 | 3.6 |
| Composite metastructure with metainterfaces | 0.5 | 0.51 | 4 | 13.58 | 1.1 | 3.7 |

Table S5. Summary of design information and relative densities for the thermos-mechanical metamaterial and its conventional counterpart designed in this work.

| Type of metamaterials | Beam diameter (mm) | Average relative densities (%) | Average normalized modulus (MPa/MPa) |
|---|---|---|---|
| Thermos-mechanical metamaterials | 0.416 | 20.7 | 0.18 |
| Conventional metamaterials | 0.5 | 20.7 | 0.17 |

266 Table S6. The hyperparameters used in FCNNs.

| Type of FCNN | FCNN for velocity prediction | FCNN for temperature prediction |
|---|---|---|
| Number of hidden layers | 2 | 2 |
| Number of neurons per layer | 50 | 30 |
| Training epochs | 2000 | 2500 |
| Activation function | ReLU | ReLU |

Table S7. The design parameters of the interfaces used in this study.

| Interface design | Parameter type | Parameter range |
|---|---|---|
| Programmable metainterface with XCT-rebuild biostructure | Stinger angle | 0 to 180 degrees |
| Interface inspired by elytra of beetle (ellipse) | Blade angle | 15 to 40 degrees |
| Interface inspired by elytra of beetle (trapezium) | Tooth width | 0.5 to 2.5 mm |
| Interface inspired by stinger of parasite | Stinger densities | 0.64 to 1.44 $mm^{-2}$ |
| Interface inspired by stinger of honeybee | Bending curvature | 1 to 2.5 $mm^{-1}$ |
| Interface modified by rectangular geometry | Size of the rectangle | 0.5 to 2.5 mm |
| Interface modified by triangular geometry | Size of triangular base | 0.5 to 2.5 mm |
| Interface modified by wavey geometry | Size of wave periods | 1 to 5 mm |

**Captions for supplementary movies**

Movie S1 (separate file). Comparison of internal fractures between metainterface with XCT-rebuild biostructures and biometric interfaces.

Movie S2 (separate file). Comparison of internal fractures for face-centered-cubic (FCC) metamaterials.

Movie S3 (separate file). Comparison of internal fractures for BCC metamaterials.

Movie S4 (separate file). Comparison of internal fractures for tesseract metamaterials.

Movie S5 (separate file). Comparison of internal fractures for SHS metamaterials.

Movie S6 (separate file). Comparison of internal fractures for vintiles metamaterials.

Movie S7 (separate file). Motion and programmed interface mechanics of robotics exoskeleton.

## References


1. H. Ayhan, N. Özyurt Koçakoğlu and S. Candan, *Microscopy Research and Technique*, 2021, **84**, 2930-2935.
2. M. Meyers, A. Lin, Y. Lin, E. Olevsky and S. Georgalis, *Jom*, 2008, **60**, 19-24.
3. Z.-L. Zhao, H.-P. Zhao, G.-J. Ma, C.-W. Wu, K. Yang and X.-Q. Feng, *Biology open*, 2015, **4**, 921-928.
4. Y. Lu, T. Ren, H. Zhang, Q. Jin, L. Shen, M. Shan, X. Zhao, Q. Chen, H. Dai and L. Yao, *Acta Biomaterialia*, 2022, **153**, 386-398.
5. M. Sahlabadi and P. Hutapea, *Bioinspiration & Biomimetics*, 2018, **13**, 036013.
6. Z. Chen, Y. Lin, W. Lee, L. Ren, B. Liu, L. Liang, Z. Wang and L. Jiang, *ACS applied materials & interfaces*, 2018, **10**, 29338-29346.
7. J. Ling, Z. Song, J. Wang, K. Chen, J. Li, S. Xu, L. Ren, Z. Chen, D. Jin and L. Jiang, *Journal of the mechanical behavior of biomedical materials*, 2017, **68**, 173-179.
8. J. Černý, F. Weyda, M. Perlík and D. Kodrík, *Microscopy and Microanalysis*, 2022, **28**, 1808-1818.
9. L. Wang, Y. Liu, Y. Yang, Y. Li and M. Bai, *Additive Manufacturing*, 2021, **42**, 101992.
10. D. Han, R. S. Morde, S. Mariani, A. A. La Mattina, E. Vignali, C. Yang, G. Barillaro and H. Lee, *Advanced Functional Materials*, 2020, **30**, 1909197.
11. S. Y. Yang, E. D. O'Cearbhaill, G. C. Sisk, K. M. Park, W. K. Cho, M. Villiger, B. E. Bouma, B. Pomahac and J. M. Karp, *Nature communications*, 2013, **4**, 1702.
12. Y. Ni, H. Bai, Z. Wang, H. Liao and W. Wu, *Composite Structures*, 2023, 117220.
13. J. Rivera, M. S. Hosseini, D. Restrepo, S. Murata, D. Vasile, D. Y. Parkinson, H. S. Barnard, A. Arakaki, P. Zavattieri and D. Kisailus, *Nature*, 2020, **586**, 543-548.